Charge Density Wave Transitions and Transport Properties of η-Mo_4O_{11} Crystals

Shigeo Ōhara

Charge Density Wave Transitions and Transport Properties of η-Mo_4O_{11} Crystals

Shigeo Ōhara

Department of Materials Science, Faculty of Science,
Hiroshima University, Higashi-Hiroshima 724, Japan

Electrical resistivity ρ, Hall coefficient R_H, and thermoelectric power S have been measured over the wide temperature range 1.5-300 K for quasi-two-dimentional crystals of monoclinic η-Mo_4O_{11}, which undergoes two charge density wave (CDW) transitions at T_{c1}=105 and T_{c2}=35 K. The effect of hydrostatic pressure on the resistivity, Hall coefficient, and magneto-resistance $\Delta\rho/\rho_0$ is also studied up to 1.2 GPa. The applied pressure enhances the 1st CDW transition temperature T_{c1}, while it suppresses the 2nd one T_{c2}. The detailed analysis gives the temperature dependences of the CDW gap energies $\Delta_1(T)$ below T_{c1} and $\Delta_2(T)$ below T_{c2}, which obey a single universal curve, independent of applied pressures. The observed Hall coefficient is positive in the temperature ranges studied but the thermoelectric power is mostly negative, which indicate that the conduction carriers are due to electrons and holes. Shubnikov-de Haas oscillations are also observed in the $\Delta\rho/\rho_0$- and R_H-H curves below T_{c2}, where three main frequencies are found, which also depend on the applied pressure, indicating that the Fermi surfaces of holes and/or electrons are pressure sensitive. Based on these experimental data, together with the magnetic field dependence of R_H below T_{c2}, we have proposed a possible band scheme for conduction electrons and holes of this unique material system that have remained after the CDW transitions.

1. Introduction

Molybdenum oxides of the Magnéli phase: monoclinic η- and orthorhombic γ-Mo_4O_{11} crystals, which are primarily built up of MoO_6 octahedral slabs separated by layers of MoO_4 tetrahedra, parallel to the bc plane,[1,2] have quasi-two-dimensional structures and thus their Fermi surfaces are strongly anisotropic with cylindrical shapes elongated along the a'-axis.[3] In particular, η-Mo_4O_{11} undergoes twice the metal-semiconductor transitions at the characteristic temperatures T_{c1}=105 and T_{c2}=35 K associated with charge density wave (CDW) instabilities; diffuse X-ray and electron scattering studies show that the nesting vector at T_{c1} is Q=0.23b^*,[4] but the one at T_{c2} is not yet known. Experimentally, anomalous behaviors have been found at T_{c1} and T_{c2} in the temperature dependences of various transport properties, such as electrical resistivity, Hall coefficient, transverse magnetoresistance, thermoelectric power, and transient thermoelectric effect.[5-9] Recent band calculations for this material using a tight-binding (block-band) method[10] have shown the existence of both electron and hole pockets in the Brillouin zone, whose Fermi surfaces are two-dimensional, which favors the partial nesting of the Fermi surfaces with the nesting vector Q=0.25b^*, in good agreement with the above experiments. Furthermore, in the low temperature CDW state ($T<T_{c2}$), two periodicities f_1 and f_2 in the de Haas-van Alphen oscillations under magnetic fields up to 5 T are found (f_1=17 T and f_2=50 T;[4] f_1=17.5 T and f_2=43 T[5]), which are regarded as due to small electron and/or hole pockets. However, much less is still certain as to the nature of the Fermi surfaces of this material system.

In the present work, we have measured the dc electrical resistivity ρ (under hydrostatic pressures up to 1.2 GPa), Hall coefficient R_H, and

thermoelectric power S over the temperature range from 1.5-300 K. We have also studied R_H and transverse magnetoresistance $\Delta\rho/\rho_0$ at liquid He temperatures under hydrostatic pressures up to 1.2 GPa and magnetic fields up to 6 T. These transport data will provide us with valuable information on the nature of the Fermi surfaces of transport carriers. Taking into account available information, we shall propose a possible band scheme of this unique materials system.

2. Experimental

Crystal growth of η-Mo_4O_{11} was made by a chemical vapor transport technique in a two-zone furnace starting from a mixture of powders of MoO_2:MoO_3=1:3 using $TeCl_4$ as a transporter, in the temperature range of T_L=510 and T_H=560 °C.[7] The crystal structures and lattice parameters of this crystal were examined by X-ray diffraction to agree with the reported data;[2] a=2.46 nm, b=0.544 nm, c=0.670 nm, and β=94.4 °. The grown crystals were thin platelets elongated along the bc-plane, and the transport measurements were made on the cleaved crystals (typically 2 × 0.5 × 0.1 mm^3). In particular, the dc electrical resistivity measurements along the c-axis were made using mechanically polished samples. The crystal orientation was determined by X-ray Laue patterns.

The galvanomagnetic measurements under magnetic fields up to 2.0 T using an electromagnet applied along the a'-axis were performed using a conventional dc potentiometric method over the temperature range from 1.5-300 K. The thermoelectric power measurements were also carried out in the same temperature range as above with a usual technique. The pressure effects on the electrical resistivity over the temperature range from 4.2-300 K and Hall coefficient and transverse magnetoresistance at 4.2 K under

the magnetic fields up to 6.0 T with a superconducting magnet were measured up to 1.2 GPa using a nonmagnetic clamp-type pressure cell (Be-Cu and SiAlON).[8] The various transport properties of these crystals depend on sample-to-sample, due to different amounts of various lattice imperfections produced during the crystal growth, such as oxygen vacancies, excess oxygen, dislocations, impurities, etc., so that we specify a sample by the value of its resistivity along b- and c-axes at room temperature $\rho_{bR}(0)$ and $\rho_{cR}(0)$, respectively (see figure captions and Table 1).

3. Experimental Results and Discussions

3.1 DC Transport Quantities at Ambient Pressure

The temperature dependence of the electrical resistivities ρ_b and ρ_c for monoclinic η-Mo_4O_{11} along b- and c-axes at ambient pressure is illustrated in Figs. 1(a) and (b), respectively. As can be seen clearly from Fig. 1(a), this material undergoes the CDW-related transitions at two distinct temperatures T_{c1}=105 and T_{c2}=35 K. In the case of the c-axis resistivity [Fig. 1(b)], only a small shoulder is observed at the second transition temperature T_{c2}. The inset shows the temperature variation of the ratios of the c-axis resistivity ρ_c to the b-axis one ρ_b, ρ_c/ρ_b. We note that in the metallic region ($T>T_{c1}$; normal state) the resistivity anisotropy is temperature independent, whereas in the CDW state below T_{c1} it is enhanced, attaining a maximum near T_{c2}, which indicates that the electronic anisotropy is appreciable after the CDW transition below T_{c1} due to the nesting of the Fermi surfaces of conduction carriers.

As shown later (Fig. 15), the Hall coefficients of η-Mo_4O_{11} in the CDW states depend strongly on an applied magnetic field H, while in the

normal state they are field independent. In order to see an overall behavior, here we shall show the Hall effect data taken at the field of 2.0 T. Figure 2 shows the temperature dependence of the Hall coefficient R_H at 2.0 T for the typical samples of η-Mo_4O_{11} [No. b1 (squares) and c1(circles)], where the electrical currents were passed along the b- and c-axes, respectively, as done for the resistivity measurements. At high temperature $T>T_{c1}$ the Hall coefficients of both crystals are very small but not zero ($R_H \sim 10^{-4}$ cm^3/C) and almost temperature independent. With decreasing temperature R_H sharply increases just below T_{c1}, levels off to nearly a constant value ($\sim 10^{-2}$ cm^3/C), and continue to increase again below its second CDW transition temperature T_{c2}, followed by approaching a constant value ($\sim 5\times 10^{-1}$ cm^3/C) at low temperature. It should be noted that there is no appreciable difference in R_H for the b- and c-axes, in sharp contrast to their resistivities (Fig. 1). The positive sign of R_H indicates conduction "holes" contributing to the dc transport.

The Hall mobilities μ_H ($=R_H/\rho$) for the above samples are plotted as a function of temperature in Fig. 3. With lowering of temperature the appreciable increases in μ_H are seen near T_{c1} and T_{c2}; at high temperatures μ_H are of the order of 1 cm^2/Vs, but at low temperatures they are exceedingly enhanced by 10^4 times as large as those at $T>T_{c1}$. Also we note that μ_H is strongly anisotropic below T_{c1} (CDW state).

In contrast to the positive Hall coefficient observed over the whole temperature range studied, the thermoelectric power S of these crystals is almost negative, except at low temperatures. Typical results of various samples are presented in Fig. 4 for η-Mo_4O_{11} (one sample along the c-axis, No. c2, and two samples along the b-axis, No. b2 and b3). At high temperatures $T>T_{c1}$ (normal state), all crystals show a linear dependence of S on temperature, and below T_{c1} the thermoelectric power is enhanced,

followed by a gradual decrease toward zero. Furthermore, with decreasing temperature the thermoelectric powers along the b-axis exhibit their sign reversals from negative to positive and vice versa. As can be seen, they are also depend on sample-to-sample. However, our overall behaviors of the S-T curves are in good agreement with the results by Guyot et al.[3)]

It should be emphasized that the thermal processes are predominantly due to electrons. At first sight, the appearance of a pronounced minimum below T_{c1} seems to be due to a phonon drag effect through a strong electron-phonon coupling, but the detailed examination of the observed S-T curves reveals that this mechanism is ruled out. Instead, the following analysis seems to be more appropriate. Since the thermoelectric powers at high and low temperatures are nearly linear to temperature T and our system is a degenerate electron system, the thermoelectric power S_e can be written by

$$S_e = -(\pi^2/3)(k_B^2/e)\xi T/E_F^e , \qquad (1)$$

where e (>0) is the electron charge, E_F^e the electron Fermi energy, and ξ a dimensionless parameter characterizing scattering mechanism; ξ=3 for phonon scattering.[11)] Assuming ξ=3, we can evaluate the Fermi energies E_{F1}^e and E_{F2}^e from the slopes of the S-T curves at high and low temperatures, respectively. As listed in Table 1, the estimated values of E_{F1}^e are of the order of a few electron volts, which are one order of magnitude as large as E_{F2}^e; Guyot et al. have underestimated $E_{F1}^e \sim 0.5$ eV with ξ=1.[3)] Such a drastic decrease in the electron Fermi energy is considered to arise from the CDW transitions due to nesting of the electron Fermi surface.

Furthermore, we should note that the thermoelectric powers below T_{c2} show a sign reversal from negative to positive or vice versa (Fig. 4),

which strongly suggests that positive holes are also responsible for the thermal process. Considering the appreciable increase in the (positive) Hall coefficients of η-Mo_4O_{11} with decreasing temperature $T<T_{c2}$ (indicating the decrease in the number of conduction holes), we may infer that the nesting of the hole Fermi surface takes place through the second CDW transition at T_{c2}, thereby accompanying the formation of the energy gap of the hole band. Thus it is expected that the hole Fermi energy $E_F{}^h$ also changes drastically at T_{c2}. In our picture, the hole system is also degenerate, and then its thermoelectric power S_h is expressed in the form $S_h=+(\pi^2/3)(k_B{}^2/e)\xi T/E_F{}^h$. However, it is difficult to estimate the values of $E_F{}^h$ from the observed curves, since the measured thermopower S is the sum of two contributions from electrons and holes, as

$$S = (S_e\sigma_e + S_h\sigma_h)/(\sigma_e + \sigma_h), \qquad (2)$$

where σ_e and σ_h are the electronic conductivity of electrons and holes, respectively.

3.2 Effect of Pressure on the CDW Transitions

Figure 5 shows the temperature dependence of the electrical resistivities ρ_b for sample No. b4 at ambient pressure (P=0) and various pressure P up to 1.2 GPa. The resistivities ρ_b show characteristic minima at the CDW transition temperatures T_{c1} and T_{c2}, indicated by arrows. With increasing pressure the first transition temperature T_{c1} and the resistivity maximum just below T_{c1} are both increased, while the second CDW transition temperature T_{c2} is shifted to a lower temperature and the resistivity maximum below T_{c2} is decreased appreciably. The variations of T_{c1} and T_{c2} with pressure P are shown in Fig. 6, where we see that T_{c1} is

increasing almost linearly with P, while T_{c2} is decreasing gradually up to about P=0.7 GPa and more drastically at high pressure P>0.7 GPa. Most of the low dimensional conductors, such as $TiSe_2$,[12] $NbSe_3$,[13] and TaS_3,[14] show a decrease of the CDW transition temperature T_c as the pressure increases, due to a change in the nesting condition. On the other hand, an increase in T_c with increasing pressure has been reported by Fujishita et al. in purple bronze $Na_{0.9}Mo_6O_{17}$.[15]

In the present work, we have analyzed the observed ρ-T curves below the transition temperatures T_{c1} and T_{c2} using the following semiempirical expressions to estimate the apparent CDW gap energies for η-Mo_4O_{11}, $\Delta_1(T)$ below T_{c1} and $\Delta_2(T)$ below T_{c2}. The electrical conductivity $\sigma_i = 1/\rho_i$ (i=1 for $T<T_{c1}$ and i=2 for $T<T_{c2}$) can be well approximated by the expression

$$\sigma_i = \sigma_{0i} + A_i \exp[-\Delta_i(T)/k_B T], \tag{3}$$

where σ_{0i} is the temperature-dependent conductivity due to normal conduction carriers, which can be empirically expressed by the following polynomial forms:

$$\sigma_{01}^{-1} = \alpha_1 + \beta_1 T \quad \text{and} \quad \sigma_{02}^{-1} = \alpha_2 + \beta_2 T + \gamma T^2, \tag{4}$$

where A_i, α_i, β_i (i=1, 2), and γ are some constants, and k_B is the Boltzmann constant. Figure 7(a) and (b) show the temperature dependences of the best-fitted values of the apparent gap energies $\Delta_1(T)$ and $\Delta_2(T)$ at various pressures P, respectively. The value of $\Delta_1(T)$ increases with lowering of temperature, and the $\Delta_1(T)$-T curve is shifted toward higher temperatures with increasing pressure. Here it is of interest to note that the $\Delta_1(T)$-T curve at P=0 is in good agreement with the temperature dependence of the satellite intensities of the X-ray diffraction for η-Mo_4O_{11} found by Guyot et al.,[4] as shown later. On the other hand, the

gap energy $\Delta_2(T)$ is also increased with decreasing temperature, whose behavior is quite different from that of $\Delta_1(T)$ [Fig. 7(a)]. These experimental results suggest that the hydrostatic pressure enhances the CDW transition at T_{c1}, whereas it suppresses the one at T_{c2}, which in turn means that the pressure induces some deformation of the Fermi surfaces and thus the change in the degree of their nestings, as well as a phonon stiffening effect.[7,8] As is well known, in an idealized one-dimensional system, the gap energy at $T=0$, $\Delta(0)$, is given by $\Delta(0)=3.5k_BT_c$,[16] where the CDW transition temperature T_c is proportional to the electron-phonon coupling constant and the lattice distortion associated with the CDW transition. Thus the observed increase in T_{c1} and $\Delta_1(T)$ by pressure indicates that the electron-phonon coupling constant and/or the lattice distortion are enhanced by the applied pressure and vice versa for T_{c2}.

In our case, however, it is impossible to obtain the values of gap energies at absolute zero $\Delta_1(0)$ and $\Delta_2(0)$ and their pressure dependence, since our empirical method of analysis is made only near T_{c1} and T_{c2}. In view of these circumstances, here we have attempted to replot the $\Delta_i(T)$-T curves at various pressures in terms of their normalized quantities, $\Delta_i(T)/k_BT_{ci}$ [rather than $\Delta_i(T)/\Delta_i(0)$] versus reduced temperature T/T_{ci} (i=1 and 2) as shown in Fig. 8. Surprisingly it turns out that all the experimental points lie on a universal curve regardless of pressure. Corresponding to Fig. 7(b), the behavior of $\Delta_2(T)/k_BT_{c2}$ near $T/T_{c2}\sim1$ is continuous, as shown in Fig. 8(b). This is because we have taken the value of T_{c2} as the temperature at which the ρ-T curve shows a resistivity minimum. Therefore, in order to fit the experimental data to the universal curve of Fig 8(a) [shown in Fig. 8(b) by the dashed curve], we must redefine the value of T_{c2} as T_{c2}' ($=0.85T_{c2}$). Figure 9 shows the normalized gap energies $\delta=\Delta_1(T)/k_BT_{c1}$ or $\Delta_2(T)/k_BT_{c2}^*$ plotted as a function

of the reduced temperature t=1-T/T_{c1} or 1-T/T_{c2}' for our sample in logarithmic scales, where the normalized satellite intensities of X-ray diffractions, I/I_0, for η-Mo_4O_{11}[4] and $(NbSe_4)_3I$[17] are also included for comparison. It is clear that our experimental data lie on a straight line with the slopes α=0.5 to 0.7 for t>0.1 and α=1.0 for t<0.08, in qualitative agreement with the X-ray diffraction data. Moreover, we see that the extrapolated value of the normalized gap energy δ to absolute zero (t=1) is $\delta\sim$3.5, which is in good agreement with the universal value predicted by BCS theory. At any rate, it turns out that our redefinition of T_{c2} by T_{c2}' is regarded as the "precursor" of the second CDW transition, where some CDW fluctuations occur.

Such a universal curve can be reasonably understood by conventional mean-field theory (α=0.5 for $0\leq t\leq 1$) and more generally by the Landau theory which predicts α=0.5 for $t\sim$1 and α=1 for $t<<1$. We have tried to compare our experimental data with the temperature dependence of the order parameter of the Landau theory defined by the following equation,

$$\delta = -A + (A^2 + Bt)^{0.5}, \qquad (5)$$

where A and B are some constants. The calculated curve with the best-fitted values A=0.19 and B=14.2 is indicated by the dashed line in Fig. 9. In our case the experimental points derive from the curve at lower reduced temperature t<0.05; more detailed measurements near the transition temperatures will be required to confirm the validity of Eq. (5).

3.3 Quantum Oscillations in the DC Transport Quantities

In the low temperature CDW state ($T<T_{c2}$), it has been reported that two periodicities in the de Haas-van Alphen oscillations under magnetic

field are observed,[4,5] which arise from the conduction carriers of small electron and/or hole pockets that are remained after nesting of their Fermi surfaces. In Fig. 10, the transverse magnetoresistance $\Delta\rho/\rho_0$ at 4.2 K is shown with increasing (solid lines) and decreasing (dashed lines) magnetic field up to 6 T at constant pressures P. As can be seen, $\Delta\rho/\rho_0$ increases with H attaining a value as large as about 12 at H=6 T, and the $\Delta\rho/\rho_0$-H curve shows an oscillatory behavior (Shubnikov-de Haas oscillations); in addition, we see a noticeable hysteresis near each maximum of the $\Delta\rho/\rho_0$-H curves. As the pressure is increased, the magnitude of the $\Delta\rho/\rho_0$-H curves is decreased and the maximum positions (indicated by arrows in Fig. 10) are also shifted. It should be also noted that the hysteresis at P=1.0 GPa is reversed compared to that at P=0.

On the other hand, the magnetic field dependence of the Hall voltages V_H at 4.2 K under ambient pressure P=0 and P=1.0 GPa is shown in Fig. 11. We see that the Hall voltages are positive and also exhibit oscillatory and small hysteresis behavior with varying magnetic field.

We have analyzed the oscillatory components in the $\Delta\rho/\rho_0$- and V_H-H curves in a semiempirical way, as given below. The observed resistive or Hall voltage $V(H)$ is regarded as the sum of an oscillatory component $V_{osc}(H)$ and a background $V_{BG}(H)$,

$$V(H) = V_{osc}(H) + V_{BG}(H), \tag{6}$$

where the background component $V_{BG}(H)$ is calculated by a successive smoothing (or averaging) procedure, with a magnetic field interval ΔH, from i=-n to n, as expressed in the following form:

$$V_{BG}(H) = (2n + 1)^{-1} \sum_{i=-n}^{n} V(H+i\Delta H). \tag{7}$$

Figure 12 shows one of the results for the oscillatory component of the Hall voltage $V_{osc}(H)$ for sample b4 at ambient pressure plotted against the reciprocal magnetic field. Here we have taken the magnetic field interval ΔH=0.04 T and n=5 for the data analysis. We can see two types of oscillatory characteristic of the Shubnikov-de Haas (SdH) phenomena.

In order to obtain the fundamental frequency components f_i (i=1, 2,...) of the SdH oscillations, we have further analyzed these $V_{osc}(H)$-$1/H$ curves using a fast Fourier transform method. The results are shown in Fig. 13 for the Hall voltages of sample b4 at different pressures; each peak in these profiles shifts toward higher frequency with increasing pressure P. Figure 14 illustrates some of the most probable components thus obtained from the magnetoresistance (solid symbols) and Hall data (open symbols) plotted against applied pressure P. It is to be noted that at low pressures P<0.5 GPa three types of frequencies (solid lines) are observed, the middle of which is undetectable at higher pressure above 0.7 GPa, and an additional frequency component (dashed line) begins to appear above 0.5 GPa; of the three fundamental frequencies observed at P=0, the only one of f=16 T is in close agreement with f=17.5 or 17 T obtained from the de Haas-van Alphen oscillations by other workers.[4,5] The effect of pressure on f_i is appreciable at high pressures P>0.7 GPa.

The above result and the pressure dependence of T_{c2} [Fig. 6(b)] may suggest that this material undergoes some pressure-induced structural change or phase transition at the characteristic pressure P_c=0.5-0.7 GPa, thus leading to an appreciable change in the shape of Fermi surfaces. Even though we cannot assign each frequency f_i to a respective origin from these data alone, we may evaluate the magnitude of cross section S_F for the extrema of electron and/or hole Fermi surfaces perpendicular to the magnetic field (or b*c*-plane) using $S_{Fi}=(2\pi)^2 e f_i/\hbar$ ($\hbar$: Plank constant);

at P=0 the value of S_{Fi} are of the order of (5-15) $\times 10^{18}$ m^{-2} that corresponds to only 0.05-0.15 % of the areas of the first Brillouin zone S_{BZ} (=1.1 $\times 10^{20}$ m^{-2}). Such small cross-sectional areas are the result of the successive nesting of the Fermi surfaces caused by two CDW transitions, and Fig. 14 shows that the resultant Fermi surfaces are strongly pressure-sensitive.

3.4 Magnetic Field Dependence of the Hall Coefficient

Finally, we shall show the magnetic field dependence of Hall coefficient R_H up to 6 T; a typical result for sample b4 at 4.2 K is shown in Fig. 15, where quantum (SdH) oscillations are clearly observed. We note that R_H is increased steeply with increasing magnetic field attaining a constant value at high field region at least up to 6 T. Such a magnetic field dependence of the Hall coefficient R_H except for SdH oscillations, can be understood in terms of classical transport expressions for multiple conduction carriers (electrons and holes) as given below.

Based on the band model developed by Canadell et al.,[10] various dc transport by Inoue et al,[7] and dynamic measurements by Sasaki et al.[9] for η-Mo_4O_{11}, a possible nesting model and band scheme of η-Mo_4O_{11} have been proposed.[7] The basic idea is that the dc transport properties of the quasi-two-dimensional conductor η-Mo_4O_{11} below the second CDW transition temperature T_{c2} (=35 K) are primarily due to the "electrons" and "holes" in the respective bands that have remained after the CDW transitions. We have attempted to carry out numerical calculations of the magnetic field dependence of the Hall coefficients using a classical expression; here we have neglected a quantum effect such as SdH oscillations. Corresponding to the three frequencies f_i of the SdH oscillations

(Fig.13), we have used a simplified three-carrier model, in which two electron bands and one hole band are taken into account, with a carrier concentration n_i and carrier mobility μ_i for the i-th band; i=1 and 2 for electron bands (hereafter denoted by e_3- and e_4-bands, respectively) and i=3 for hole band (h_3-band).

Then the Hall coefficient R_H is given by

$$R_H(H) = N(H)/(A(H)^2 + N(H)^2 H^2), \tag{8}$$

with

$$N(H) = \sum_{i=1}^{3} n_i e\mu_i^2/(1+\mu_i^2 H^2), \tag{9}$$

$$A(H) = \sum_{i=1}^{3} n_i |e|\mu_i/(1+\mu_i^2 H^2), \tag{10}$$

with the electronic charge e ($e<0$ for electron and $e>0$ for hole). The calculated R_H-H curve for sample b4 is indicated by solid line in Fig. 15 with the best-fit values of $n_1=1.7\times10^{18}$, $n_2=2.8\times10^{17}$, $n_3=6.1\times10^{18}$ cm^{-3}, $\mu_1=4.2\times10^4$, $\mu_2=1.7\times10^5$, and $\mu_3=5.9\times10^4$ cm^2/Vs, in good agreement with the experimental curve. Corresponding to the observed carrier concentration p_H determined from the Hall coefficient at 2.0 T ($p_H=1/eR_H$) shown in Fig. 2, the evaluated hole concentration n_3 of the hole h_3-band has the higher value compared with those of electrons (n_1 and n_2), which indicates that the main contribution of carrier transport is due to conduction holes. The conduction electrons of the e_3- and e_4-bands are also responsible for the transport, since their evaluated electron mobilities μ_1 and μ_2 are comparatively high, even though their concentrations are lower than the hole one. Thus one may conclude that there are at least two types of electron bands and one hole band contributing to dc transport in the CDW

state; furthermore we have found two types of hole bands and two types of electron bands, as found by Sasaki et al.[9]

4. Band Scheme and Nesting Model

From the experimental results and discussions described above, we shall now propose a tentative band scheme for η-Mo_4O_{11} with quasi-two-dimensional layered structures. In this material system, both electrons and holes are degenerate and contribute to the various anisotropic transport phenomena. Furthermore, these carrier systems undergo the normal-to-CDW transitions through nestings of the Fermi surfaces, at which the pressure effect is appreciable and the transport anisotropy is enhanced.

As shown schematically in Fig. 16(a), in the normal state ($T>T_{c1}$) electrons in the electron band (abbreviated by e-band) are filled up to E_{F1}^{e} and holes in the hole band (h-band) up to E_{F1}^{h}, just like a semimetal. These carriers are mobile in each band having different effective masses and drift mobilities. After the first CDW transition ($T_{c2}<T<T_{c1}$) due to nesting of each Fermi surface by an amount of $2k_F$ (k_F: the Fermi wave vector), each band is split into two bands [Fig. 16(b)]; for electrons, a "vanishing" or "nested" band (e_1-band) with a gap energy Δ_1^{e}, which does not contribute to the conduction at absolute zero (insulating), and a "remaining" band (e_2-band) with the Fermi energy E_{F2}^{e} ($<<E_{F1}^{e}$), which contribute to the conduction with a drift mobility and effective mass that may be different from those of the original e-band. Similarly the h-band for holes will be split by nesting into a vanishing h_1-band with a gap Δ_1^{h} and a remaining h_2-band with the hole Fermi energy E_{F2}^{h}; the values of E_{F1}^{h} and E_{F2}^{h}, however, are not obtainable from the

measurements done so far. According to our analysis of the R_H-H curve (Fig. 15), the simplified remaining band scheme for η-Mo_4O_{11} at the CDW states ($T<T_{c2}$) can be represented schematically as Fig. 16(c), which consist of the h_3-band for holes and the e_3- and e_4-bands for electrons.

Such changes in both electron and hole bands upon the CDW transitions are responsible for the appearance of anomalies near T_{c1} in the temperature dependence of various physical quantities, such as transport properties as shown in this work, together with the specific heats[3] and paramagnetic susceptibilities (which indicate the decrease in the density of states at the Fermi energies, too).[4] Moreover, the second CDW transition occurs probably through nesting of the Fermi surface of the "h_2-band" of holes, resulting in the splitting of the h_2-band into vanishing and remaining hole bands with the relevant band parameters, which are inferred from the drastic change in the positive Hall coefficient (Fig. 2) and the sign reversal of the thermoelectric power observed below T_{c2} (Fig. 4).

On the basis of the above band model, we propose a tentative picture of the variations of the Fermi surfaces of the electron and hole bands associated with the normal-to-CDW transitions with appropriate nesting vectors for η-Mo_4O_{11}, as shown schematically in Fig. 17 for by the first Brillouin zone in the b*c*-plane; only the nesting vector along the b*-axis $Q_b=0.23b^*$ is experimentally known.[4] Here we assume, for simplicity, that the e-band lies at the zone center [shaded region] and the h-band at the zone edges [open region], and that their nesting vectors are equal and point towards b*-axis; we denote the nesting vector by Q_{b1} below T_{c1} and Q_{b2} below T_{c2}, as indicated by arrows. Below the first CDW transition temperature T_{c1}, through an intraband nesting of the electron and/or hole Fermi surface by Q_{b1} (indicated by solid arrows) or an interband nesting

(broken arrows), each band splits into two bands; only the Fermi surfaces of the remaining bands are shown in Fig. 17. The second CDW transition takes place below T_{c2} by nesting the separated hole Fermi surfaces by an amount of Q_{b2}, resulting in further splitting into hole bands. We should note that the hole Fermi surfaces in the temperature range $T_{c2}<T<T_{c1}$ are strongly anisotropic (see inset of Fig 1).

5. Conclusion

Present studies on the CDW related transport phenomena in the quasi-two-dimentional η-Mo_4O_{11} can be summarized as follows:

1) The temperature dependences of the resistivity, Hall coefficient, Hall mobility, and thermoelectric power of η-Mo_4O_{11} have shown that these electronic properties are strongly anisotropic in the bc-plane, indicating the anisotropic Fermi surfaces of the conduction carriers.
2) The Hall coefficient R_H is positive over the entire temperature range studied, while the thermoelectric power S is almost negative, except at low temperatures. These results indicate that the conduction carriers in this material system are both "electrons" and "holes".
3) The effect of hydrostatic pressure on the electrical resistivity has shown that the first CDW transition temperature T_{c1} is increased with pressure, which is considered as due to enhanced electron-phonon interactions. On the other hand, the second CDW transition temperature T_{c2} is decreased by applied pressure, which indicates that the pressure suppresses the CDW nesting of the Fermi surfaces.
4) From the analysis of the observed $\rho(P)$-T curves, we have estimated the CDW gap energies $\Delta_1(T)$ and $\Delta_2(T)$. The temperature dependence of these gap energies can be fitted to a universal curve, in good agreement

with other experimental and theoretical results.

5) Below T_{c2}, we have found Shubnikov-de Haas oscillations in both the magnetoresistance and Hall voltage. The fast Fourier transform analysis of these oscillations gives the three main frequencies at ambient pressure (f =4.5, 7.5, 16 T), which are also found to be pressure dependent, suggesting that the Fermi surfaces of electron and/or holes are very much pressure sensitive. The extremal cross sections of the Fermi surfaces are estimated to be about 0.05-0.15 % of the first Brillouin zone area.

6) Computer simulations of the magnetic field dependence of the Hall coefficient have shown that the carrier systems can be represented by three-carrier model consisting of two types of electron bands (with carrier concentrations $n_1=1.7\times10^{18}$, $n_2=2.8\times10^{17}$ cm^{-3}, and carrier mobilities $\mu_1=4.2\times10^4$, $\mu_2=1.7\times10^5$ cm^2/Vs), and one type of hole band ($n_3=6.1\times10^{18}$ cm^{-3} and $\mu_3=5.9\times10^4$ cm^2/Vs).

7) Based on these experimental data, we have proposed a possible nesting model and a band scheme of this unique material of quasi-two-dimensional system. In order to clarify such a picture, more detailed experimental and theoretical works will be needed.

Acknowledgements

The author would like to express his sincere thanks to Professor Masasi Inoue for helpful instruction and stimulating discussions during the course of the present work. He is also grateful to Associate Professor Minoru Sasaki, Drs. Hiroshi Negishi and Mikio Koyano for fruitful discussions and useful advice. He also thanks the all members of his laboratory for their assistance.

References

1) A. Magnéli, Acta Chem. Scand. **2**, 861 (1948).

2) L. Kihlborg, Acta Chem. Scand. **13**, 954 (1959).

3) H. Guyot, C. Escribe-Filippini, G. Fourcaudot, K. Konate, and C. Schlenker, J. Phys. C **16**, L1227 (1983).

4) H. Guyot, C. Schlenker, J. P. Pouget, R. Ayroles, and C. Roucau, J. Phys. C **18**, 4427 (1985).

5) C. Schlenker, J. Dumas, C. Escribe-Filippini, H. Guyot, J. Marcus, and G. Fourcaudot, Philos. Mag. B **52**, 643 (1985).

6) C. Schlenker ed., *Low-Dimensional Electronic Properties of Molybdenum Bronzes and Oxides* (Kluwer Academic Pub., Dordrecht, Boston, Lonon, 1989) p. 159.

7) M. Inoue, S. Ōhara, S. Horisaka, M. Koyano, and H. Negishi, phys. stat. sol. (b) **148**, 659 (1988).

8) S. Ōhara, M. Koyano, H. Negishi, M. Sasaki, and M.Inoue, phys. stat. sol. (b) **164**, 243 (1991).

9) M. Sasaki, G. X. Tai, and M. Inoue, phys. stat. sol. (b) **162**, 553 (1990).

10) E. Canadell, M. H. Whangbo, C. Schlenker, and C. Escribe-Filippini, J. Inorg. Chem. **28**, 1466 (1989).

11) R. D. Barnard, *Thermoelectricity in Metals and Alloys*, (Taylor & Francis, London, 1972) P. 58.

12) N. Ogasawara, K. Nakamura, and S. Tanaka, Solid State Commun., **31**, 873 (1979).

13) A. Briggs, P. Monceau, M. Nunez-Regueiro, J. Peyrard, M. Ribault, and J. Richard, J. Phys. C **13**, 2117 (1980).

14) M. Ido, K. Tsutsumi, T. Sambongi, and N. Mori, Solid State Commun., **29**, 399 (1979).

15) H. Fujishita, C. Murayama, N. Mori, and M. Sato, J. Phys. **2**, 8751 (1990).

16) P. A. Lee, T. M. Rice, and P. W. Anderson, Phys. Rev. Lett. **31**, 462 (1973).

17) M. Izumi, T. Iwazumi, K. Uchinokura, R. Yoshizaki, and E. Matsuura, Solid State Commun., **51**, 191 (1984).

Figure Captions

Fig. 1. Temperature dependence of the electrical resistivity ρ_b and ρ_c along (a) b-axis (sample No. b1 with $\rho_{bR}(0)$=80 $\mu\Omega$ cm; squares) and (b) c-axis (sample No. c1 with $\rho_{cR}(0)$=140 $\mu\Omega$ cm; circles) of monoclinic η-Mo_4O_{11}. The inset shows the resistivity ratio ρ_c/ρ_b. The arrows indicate the CDW transition temperatures T_{c1} and T_{c2}.

Fig. 2. Temperature dependence of the Hall coefficient R_H at 2.0 T for the samples shown in Fig. 1

Fig. 3. Temperature dependence of the Hall mobilities μ_H ($=R_H/\rho$) for the samples shown in Fig. 1.

Fig. 4. Temperature dependence of the thermoelectric power S for η-Mo_4O_{11} (open circle: No. c2, open square: No. b2, solid square: No. b3); the value of $\rho_R(0)$ for each sample is listed in Table 1.

Fig. 5. Temperature dependence of the electrical resistivity ρ_b for sample b4 [$\rho_{bR}(0)$=90 $\mu\Omega$ cm] at ambient pressure (open circles) and different pressures (solid circle: P=0.4, open square: 0.8, solid square: 1.2 GPa); arrows indicate the CDW transition transition temperatures T_{c1} and T_{c2}.

Fig. 6. Transition temperatures (a) T_{c1} and (b) T_{c2} plotted against hydrostatic pressure P.

Fig. 7. Temperature dependence of the best-fit values of gap energies, (a) $\Delta_1(T)$ and (b) $\Delta_2(T)$ in Eq. (3) at various pressures P shown in Fig. 6.

Fig. 8. Normalized plots for (a) $\Delta_1(T)/k_B T_{c1}$ and (b) $\Delta_2(T)/k_B T_{c2}$ of the experimental data shown in Fig. 7 at various pressures as a function of the reduced temperature T/T_{c1} or T/T_{c2}. The dashed curve in Fig. 8(b) is the universal curve shown in Fig. 8(a).

Fig. 9. Normalized gap energies δ ($=\Delta_1(T)/k_B T_{c1}$, indicated by closed circles or $\Delta_2(T)/k_B T_{c2}$, indicated by open circles) plotted against reduced temperature t ($=1-T/T_{c1}$ or $1-T/T_{c2}$') in logarithmic scales; for comparison, the normalized satellite indicates I/I_0 of X-ray diffrations for η-Mo_4O_{11} (open square)[4] and $(NbSe_4)_3I$ (solid square)[17] are also included. The dashed curve is the theoretical one according to the Landau theory expressed by Eq. (5).

Fig. 10. Variation of the transverse magnetoresistance $\Delta\rho/\rho_0$ for sample b4 at 4.2 K with increasing (solid lines) and decreasing (dashed lines) magnetic field at constant pressures P; arrows indicate the peaks of oscillations.

Fig. 11. Variation of the Hall voltage V_H for sample b4 at 4.2 K with increasing (solid lines) and decreasing (dashed lines) magnetic field at P=0 and 1.0 GPa; arrows indicate the peaks of oscillations.

Fig. 12. The oscillation component of the Hall voltage for sample b4 at 4.2 K and ambient pressure plotted against the reciprocal magnetic field obtained by a successive averaging procedure using Eqs. (6) and (7).

Fig. 13. The fast Fourier transformed components of the Shubnikov-de Haas oscillations in the Hall voltages at various pressures P; arrows indicate the most probable frequencies f_i.

Fig. 14. Fundamental oscillation frequencies f_i vs. applied pressure P, obtained from the analysis of the oscillatory components of the $\Delta\rho/\rho_0$-H (solid symbols) and V_H-H (open symbols) curves at 4.2 K.

Fig. 15. Magnetic field dependence of the Hall coefficient $R_H(H)$ for sample b4 at 4.2 K. The solid line indicates the theoretical one calculated using Eqs. (8)-(10) with the best-fit parameters described in the text. The arrows show the maxima due to quantum oscillations.

Fig. 16. Schematic electron and hole bands for (a) normal state ($T>T_{c1}$), (b) the first CDW state ($T_{c2}<T<T_{c1}$), and (c) the second CDW state ($T<T_{c2}$) (see text).

Fig. 17. Schematic variation of the Fermi surfaces of electron band (shaded region) and hole band (open region) due to CDW transitions for η-Mo_4O_{11} with the nesting vectors along the b'-axis, as indicated by arrows (see text).

Table 1. Sample characteristics; $\rho_{bR}(0)$ resistivity along the b-axis, $\rho_{cR}(0)$ that along the c-axis of η-Mo_4O_{11} crystals at ambient pressure and room temperature, E_{F1}^{e} and E_{F2}^{e} electron Fermi energies (see text).

Sample No.	$\rho_{bR}(0)$ ($\mu\Omega$ cm)	$\rho_{cR}(0)$ ($\mu\Omega$ cm)	E_{F1}^{e} (eV)	E_{F2}^{e} (eV)
b1	80			
b2	160		4.5	0.90
b3	110		2.6	0.32
b4	90			
c1		140		
c2		190	4.1	0.18

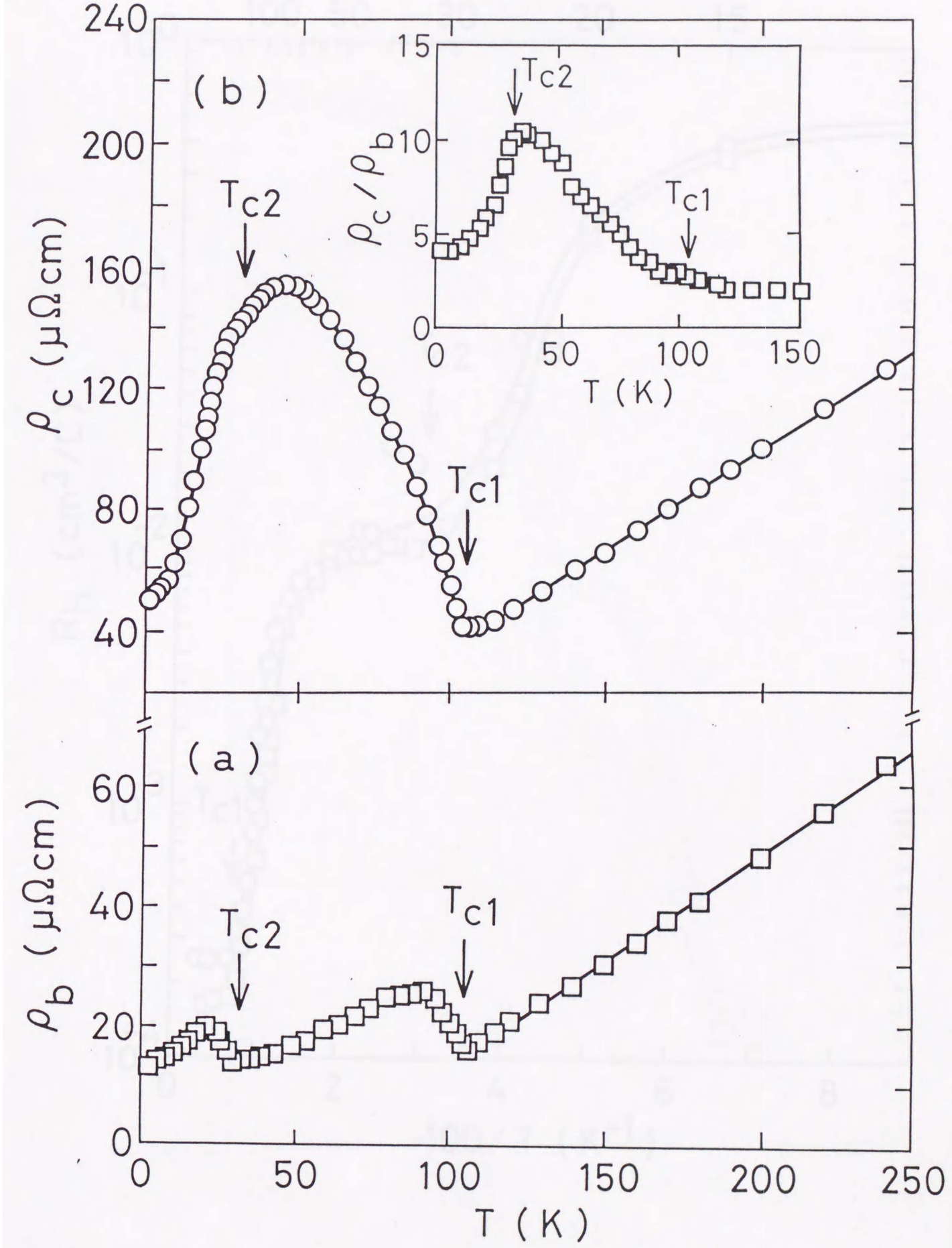
(b)
(a)
T_{c2}
T_{c1}
ρ_c (μΩcm)
ρ_b (μΩcm)
ρ_c/ρ_b
T (K)
240
200
160
120
80
40
60
20
0
50
100
150
250
15
10
5

Fig. 1

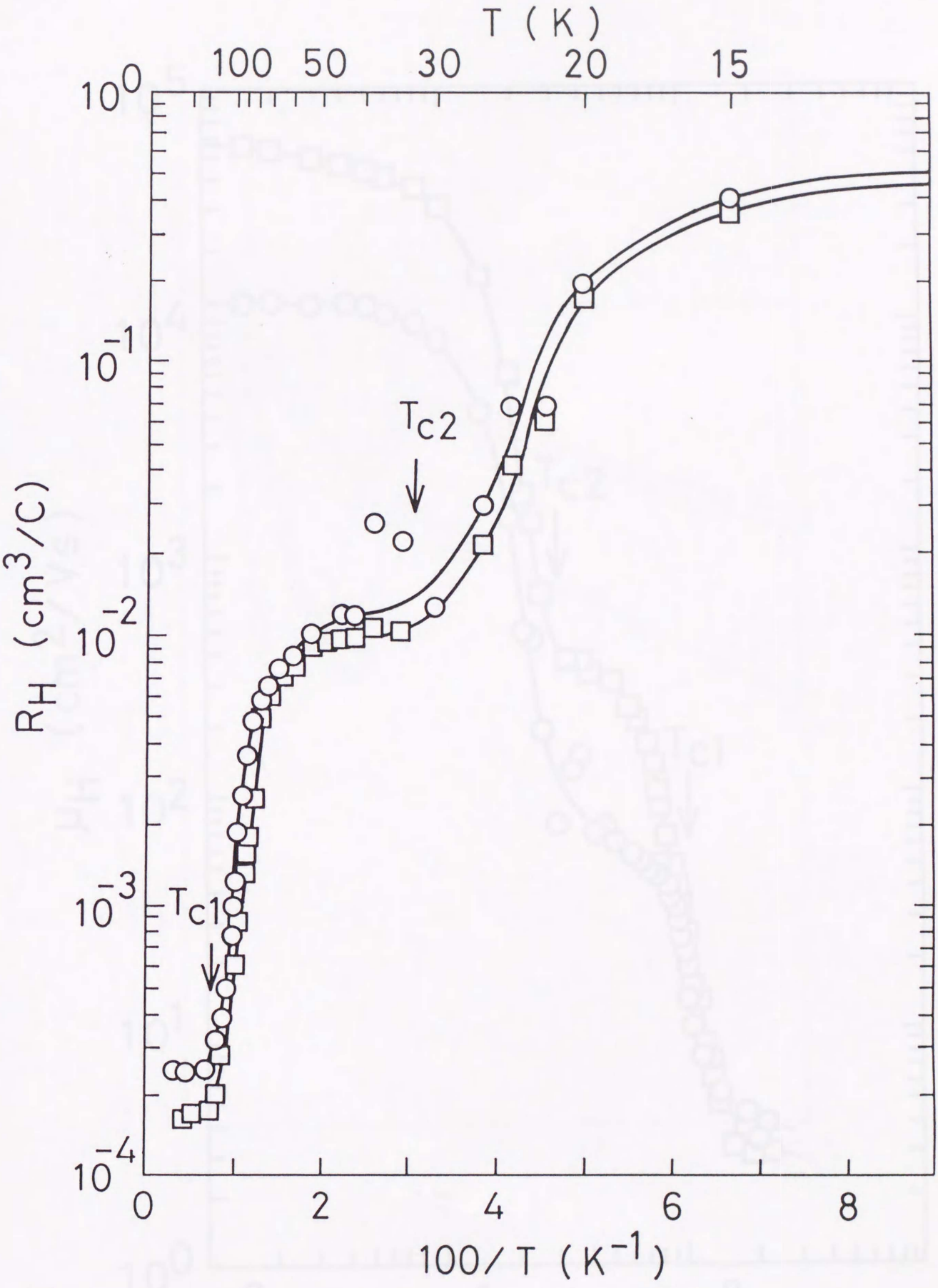
T (K)
100
50
30
20
15
10^0
10^{-1}
10^{-2}
10^{-3}
10^{-4}
R_H (cm^3/C)
T_{c2}
T_{c1}
0
2
4
6
8
100/ T (K^{-1})

Fig. 2

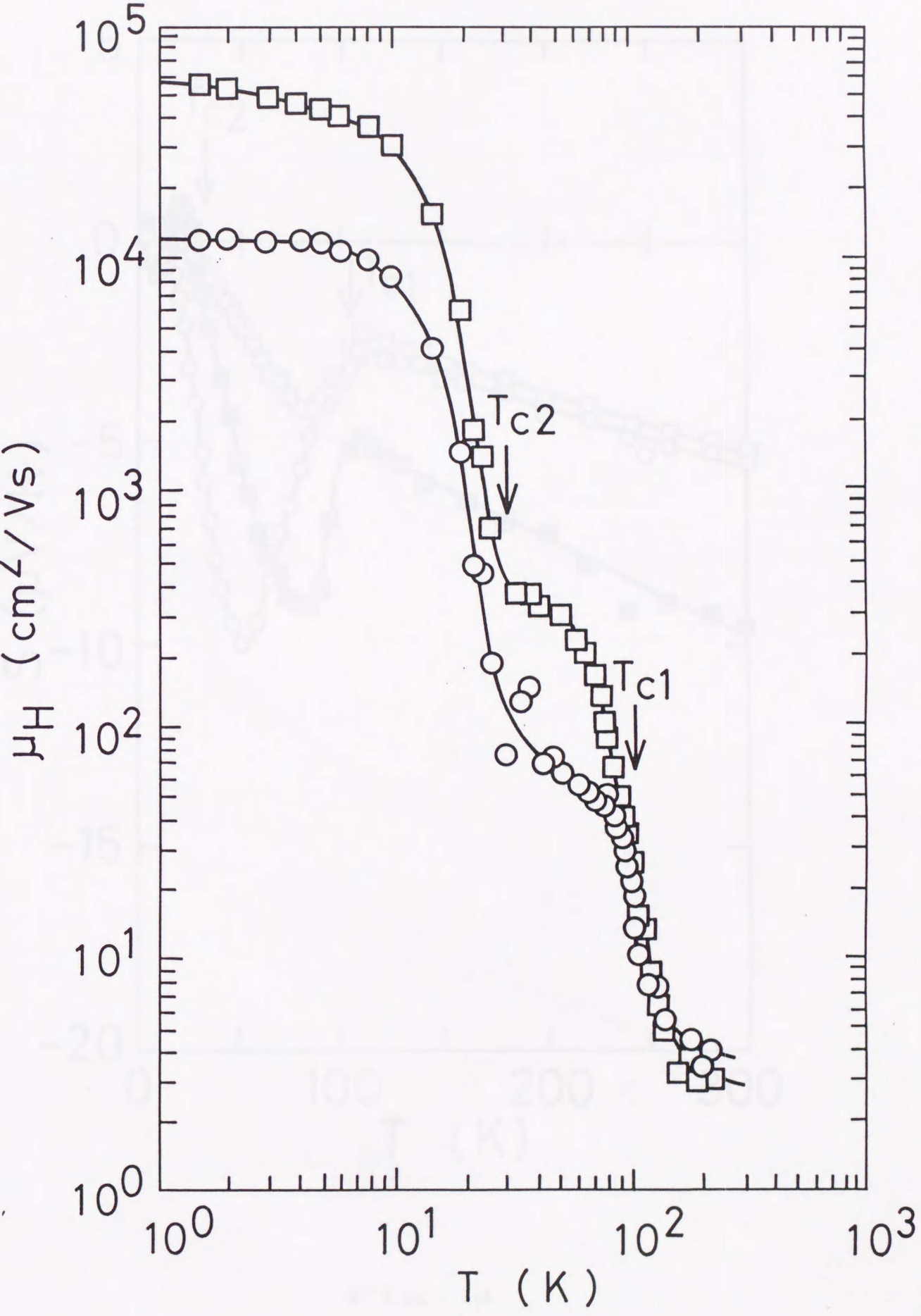

Fig. 3

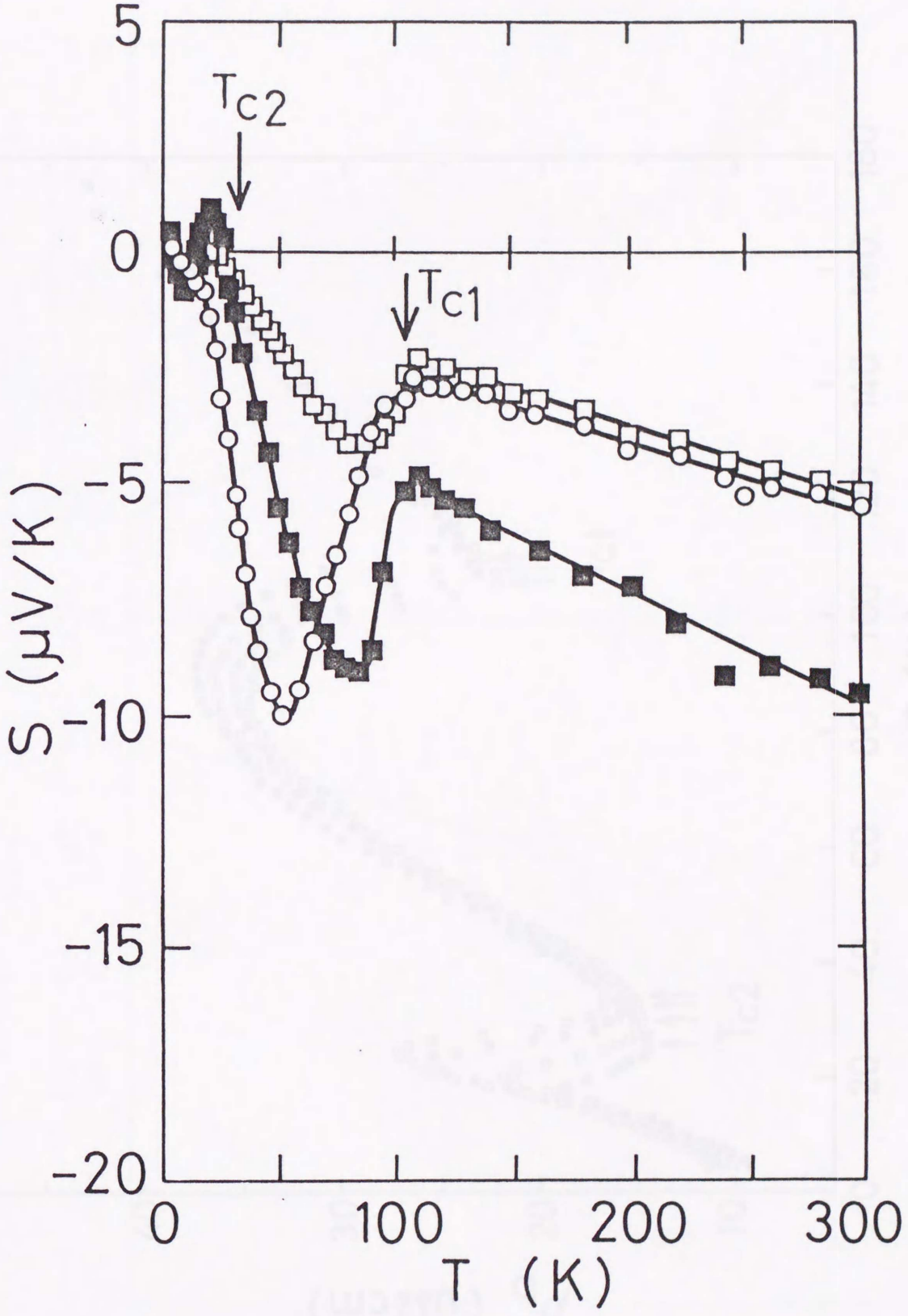

Fig. 4

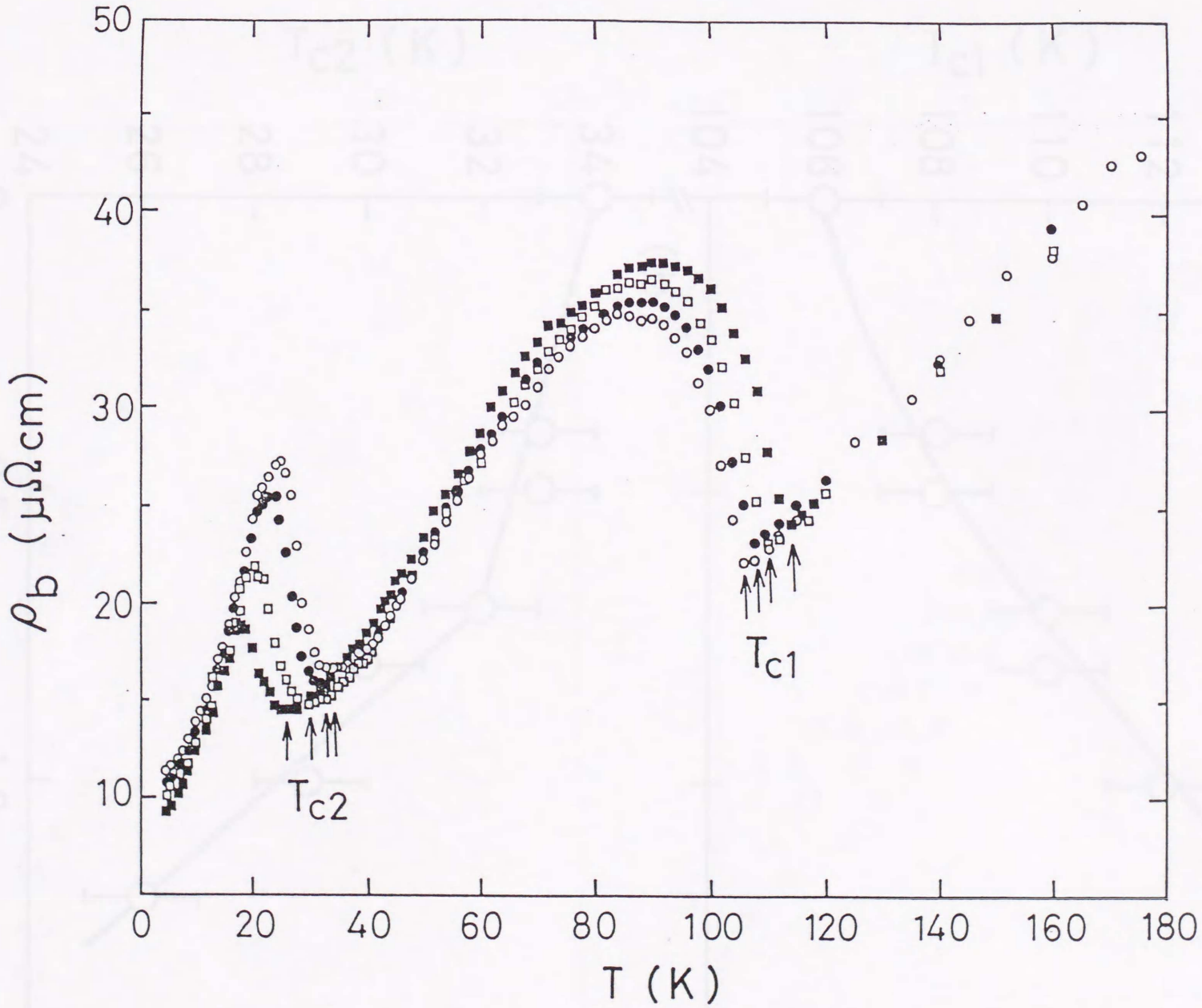
50
40
30
20
10
ρ_b ($\mu\Omega$cm)
0
20
40
60
80
100
120
140
160
180
T (K)
T_{c2}
T_{c1}

Fig. 5

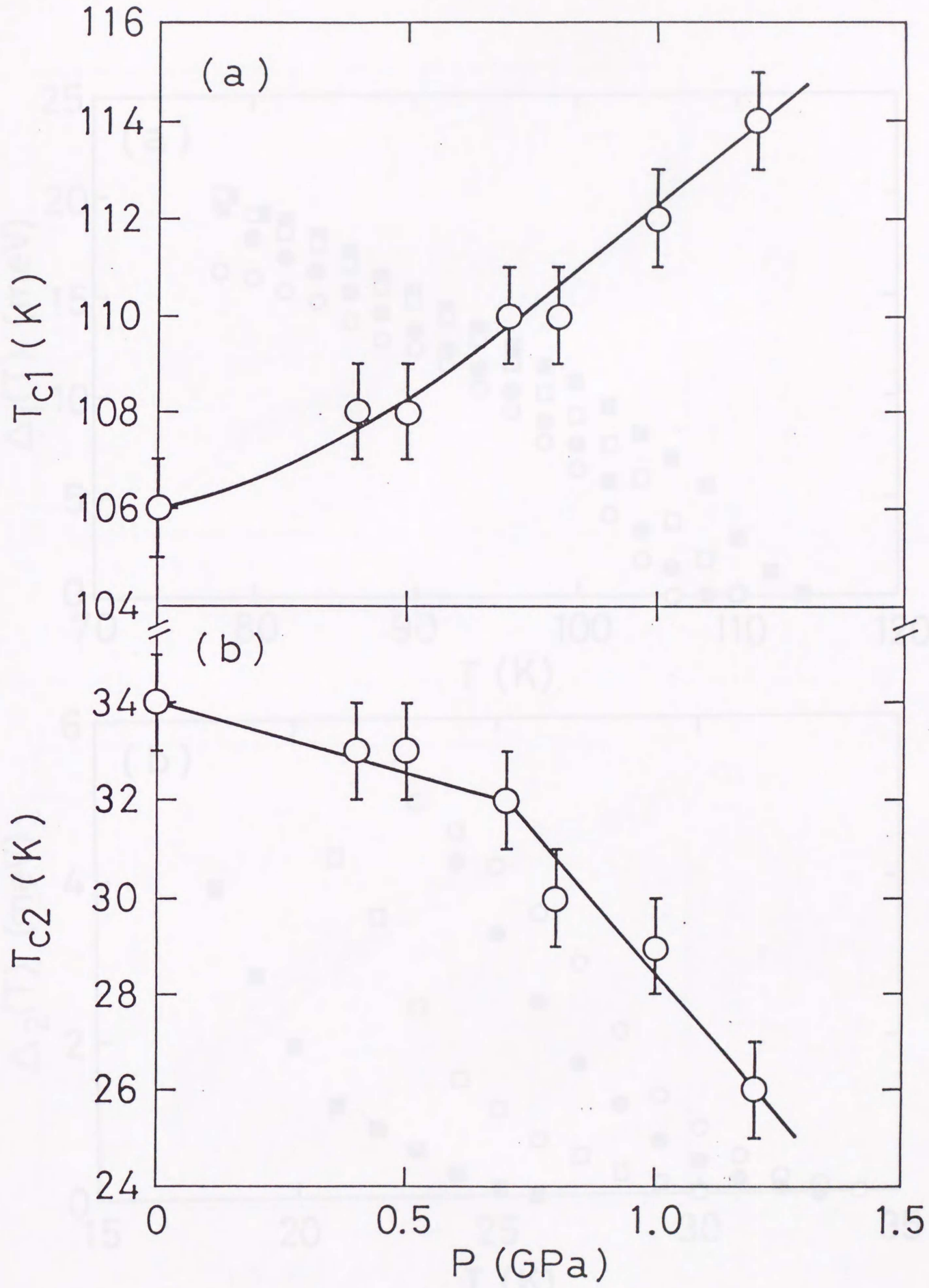
(a)
116
114
112
110
108
106
104
T_{c1} (K)
(b)
34
32
30
28
26
24
T_{c2} (K)
0
0.5
1.0
1.5
P (GPa)

Fig. 6

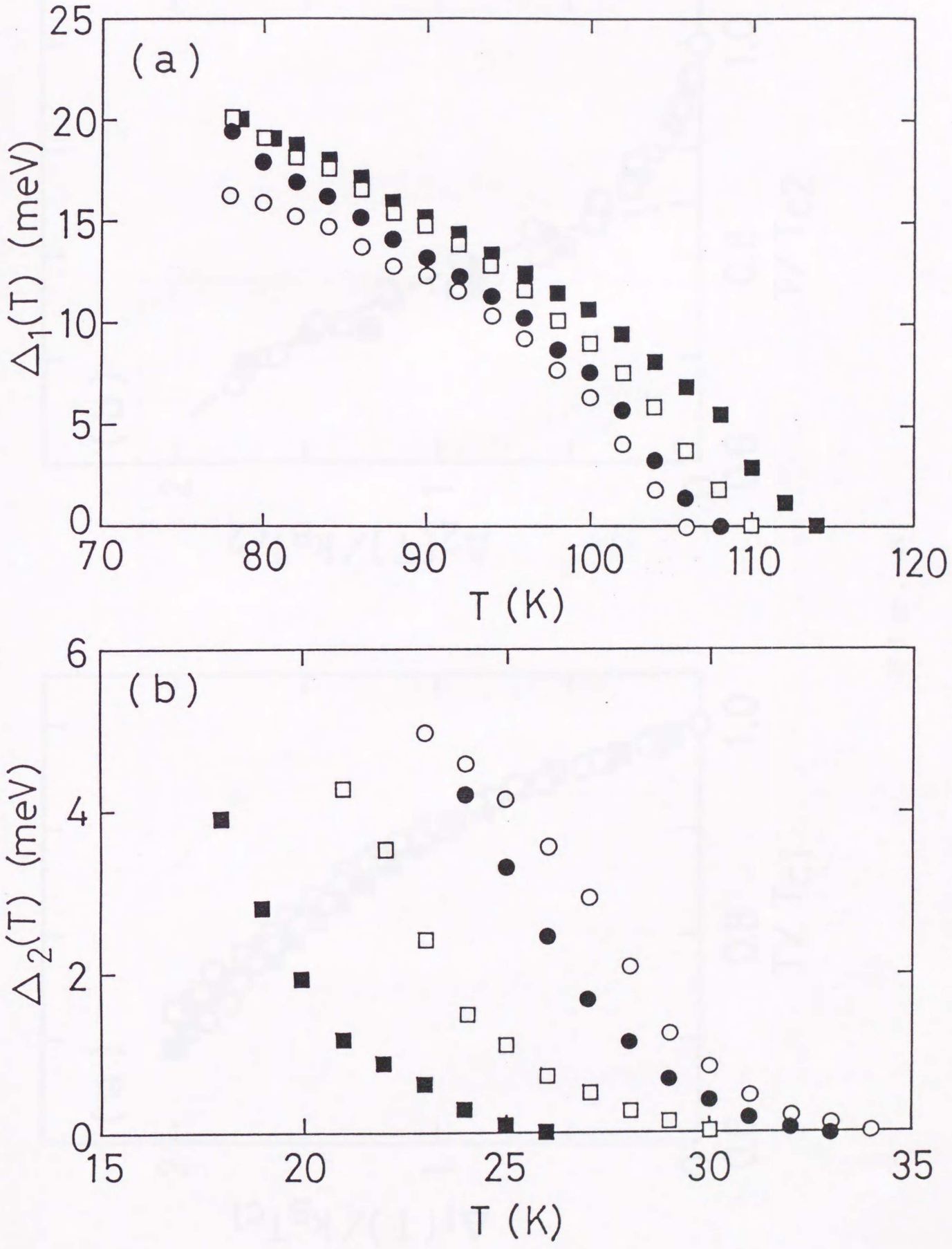
(a)
25
20
15
10
5
0
Δ_1(T) (meV)
70
80
90
100
110
120
T (K)
(b)
6
4
2
0
Δ_2(T) (meV)
15
20
25
30
35
T (K)

Fig. 7

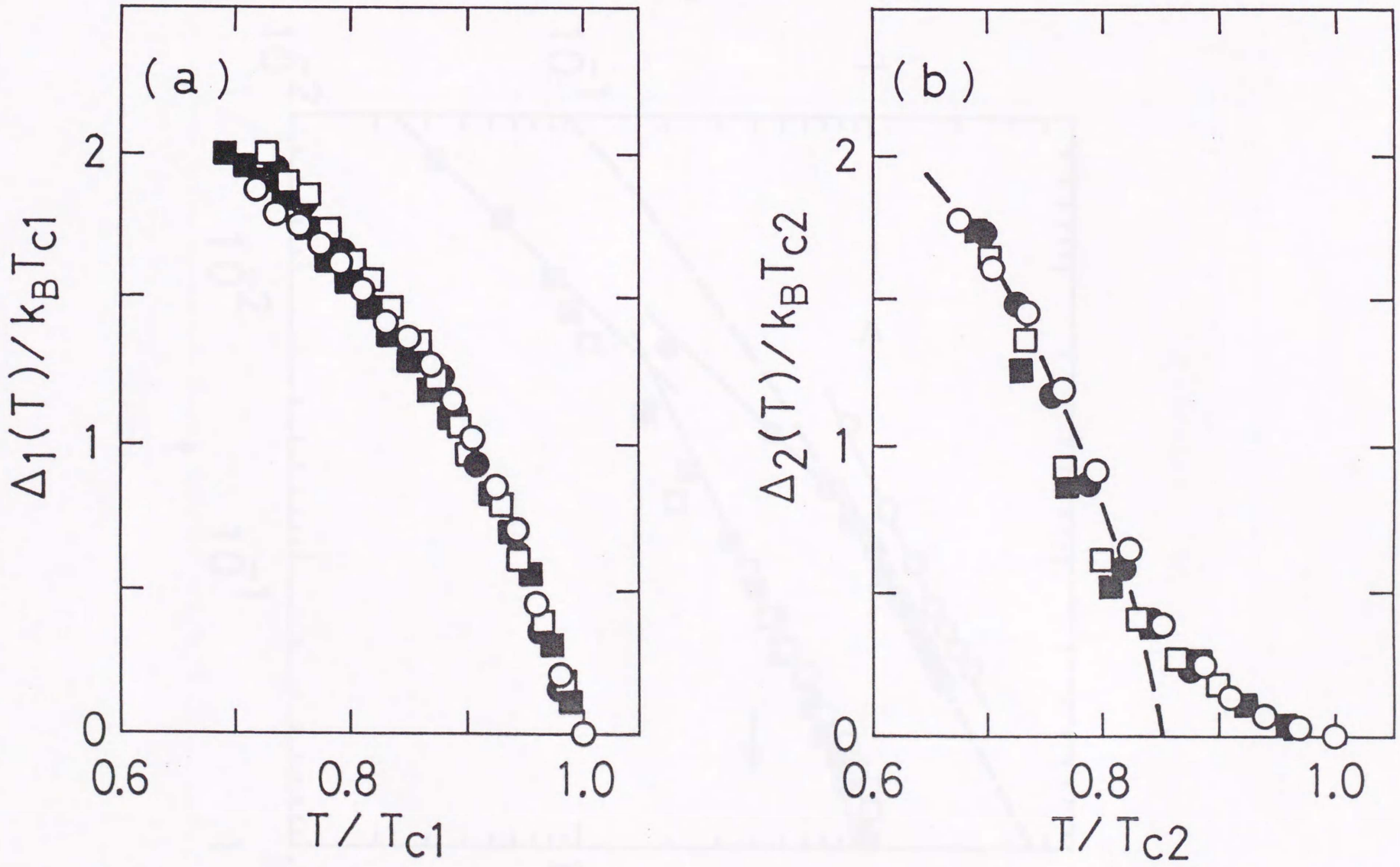

Fig. 8

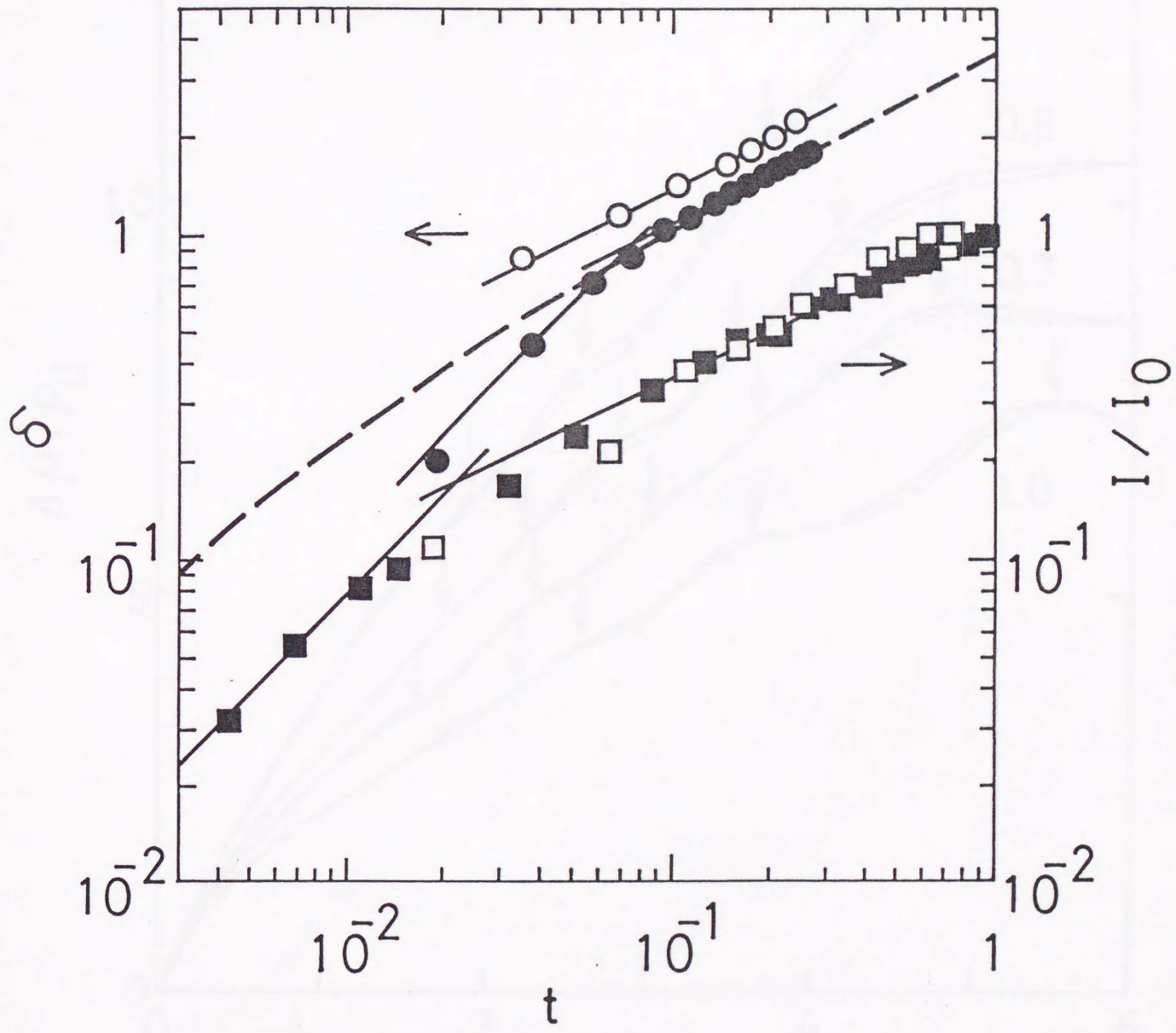

Fig. 9

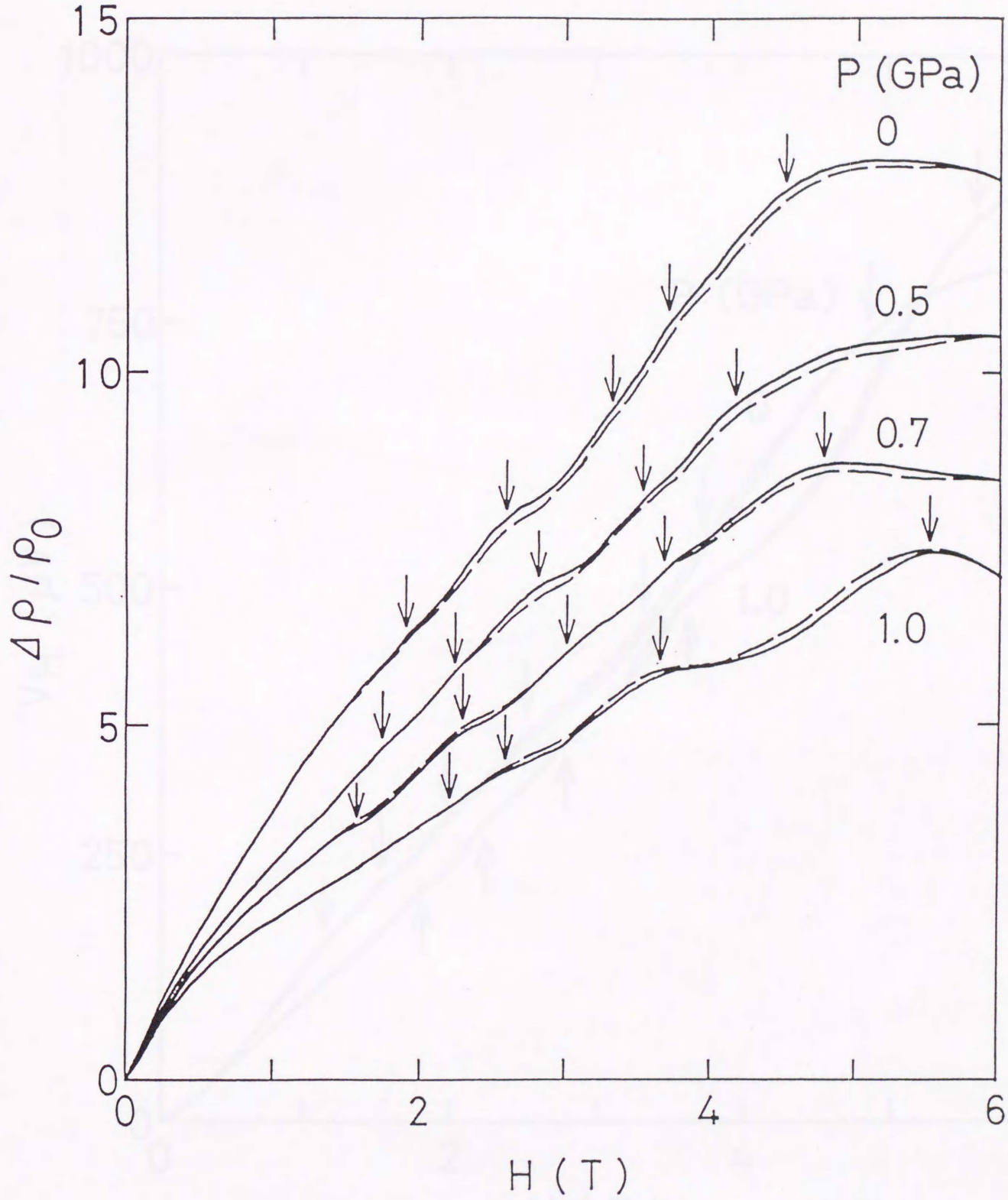

Fig. 10

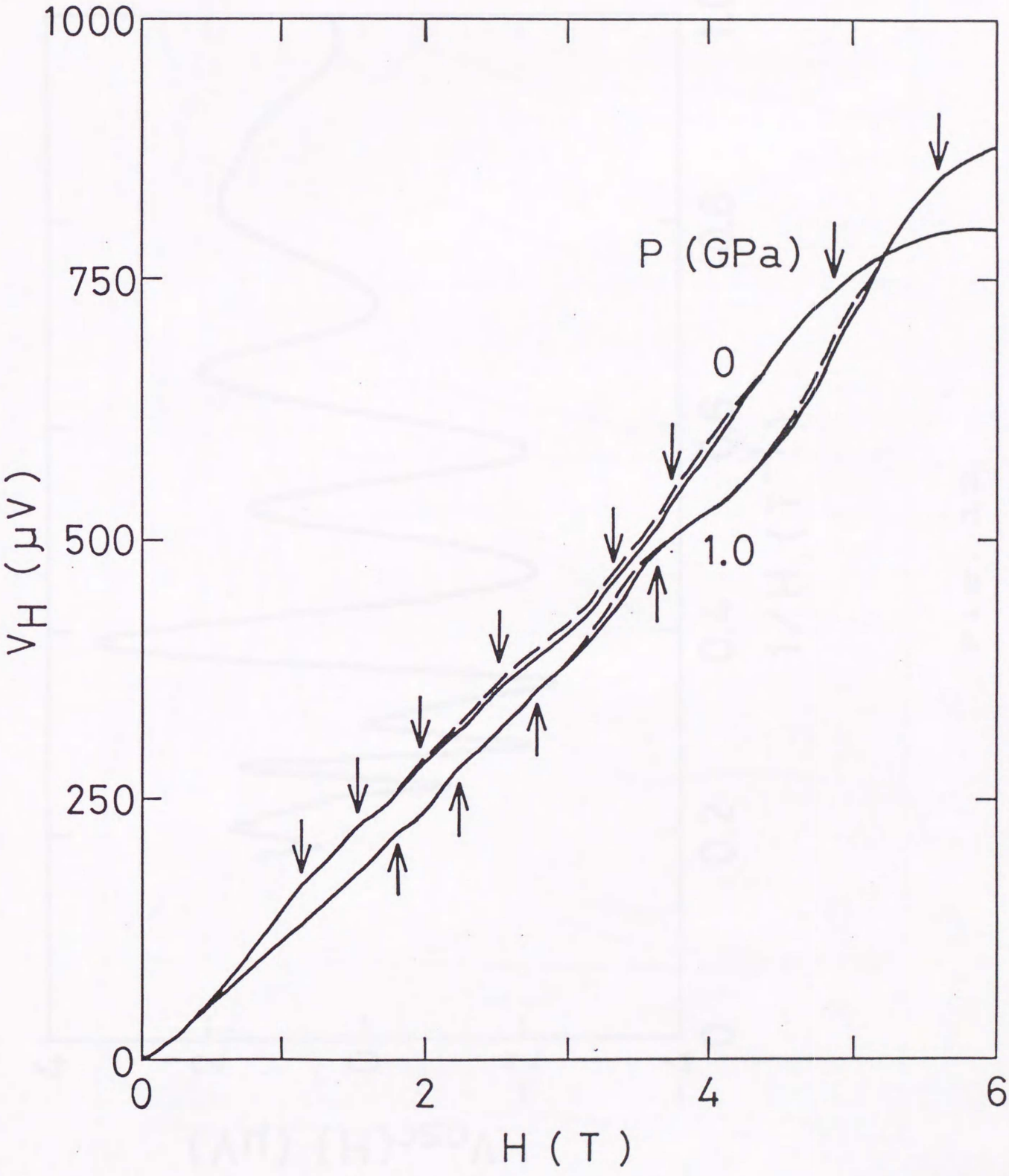

Fig. 11

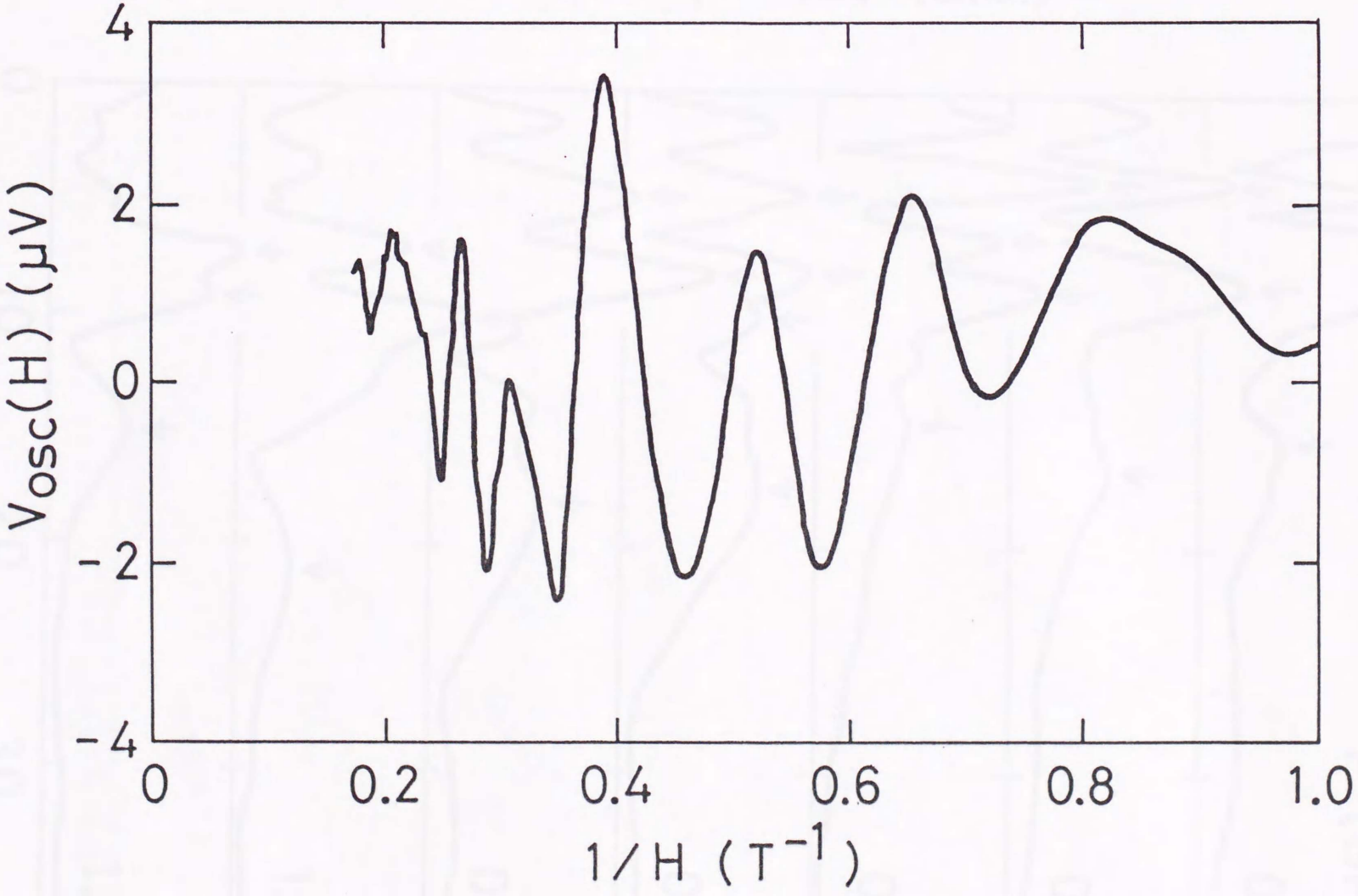

Fig. 12

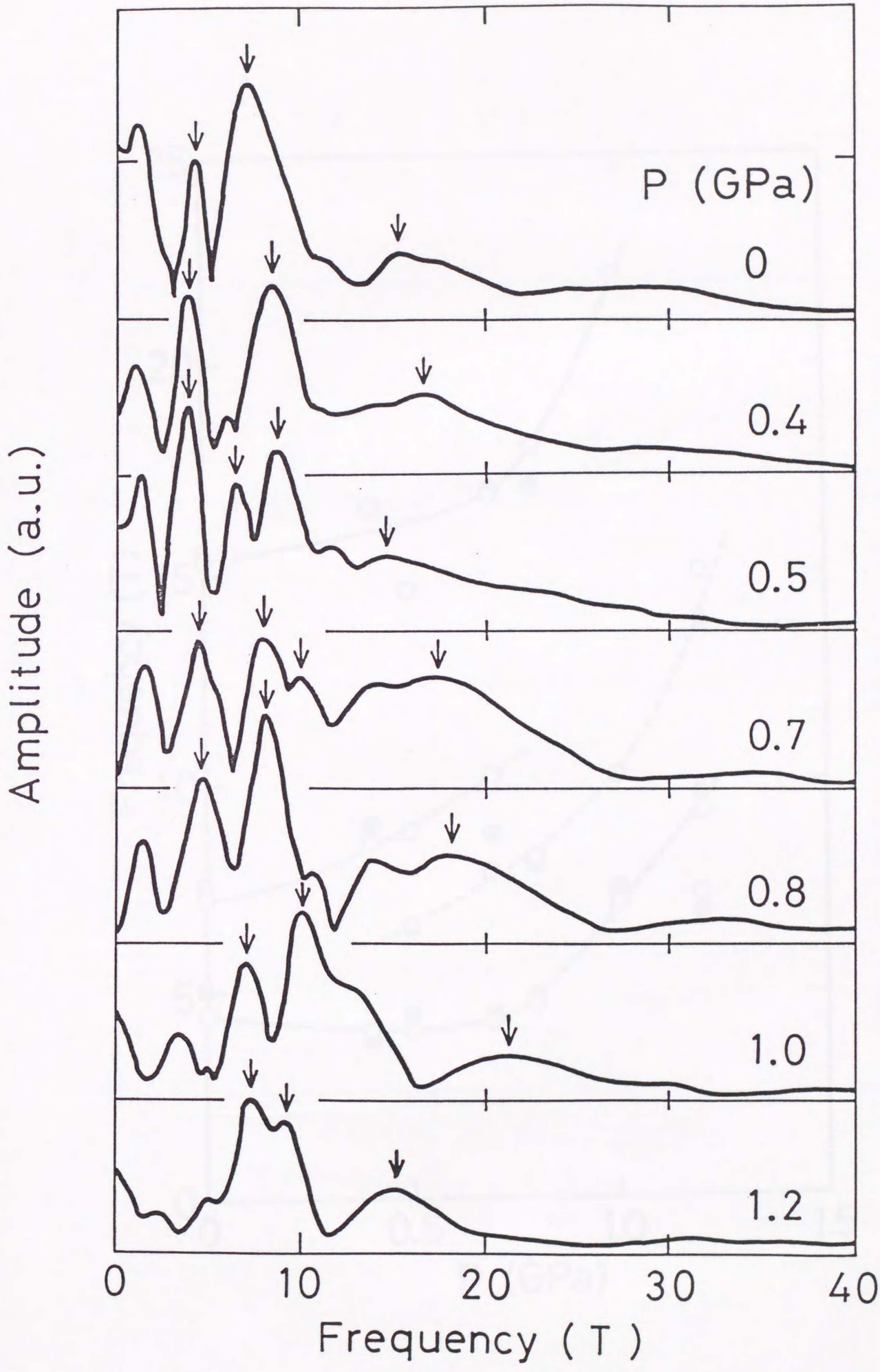

Fig. 13

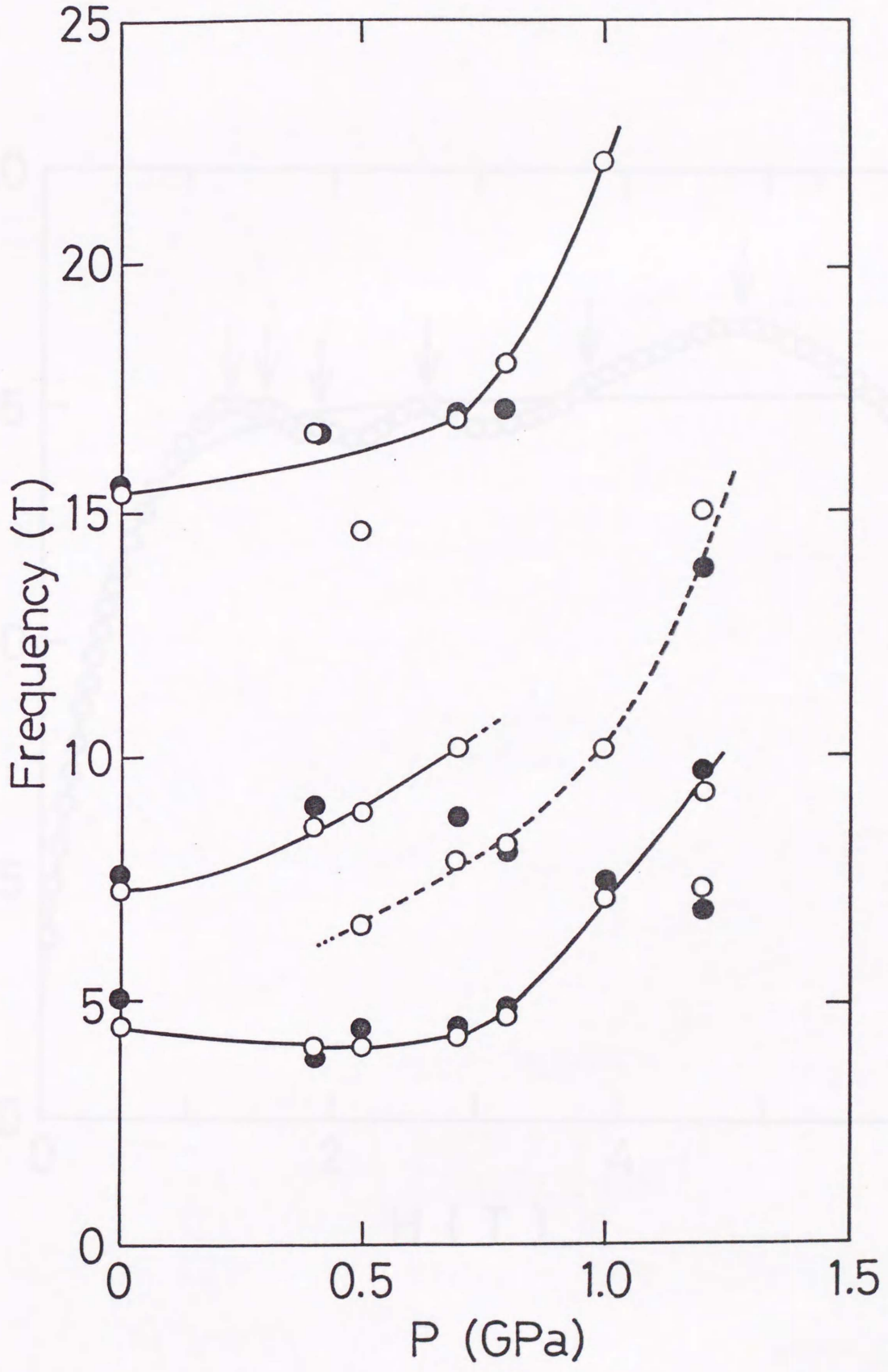

Fig. 14

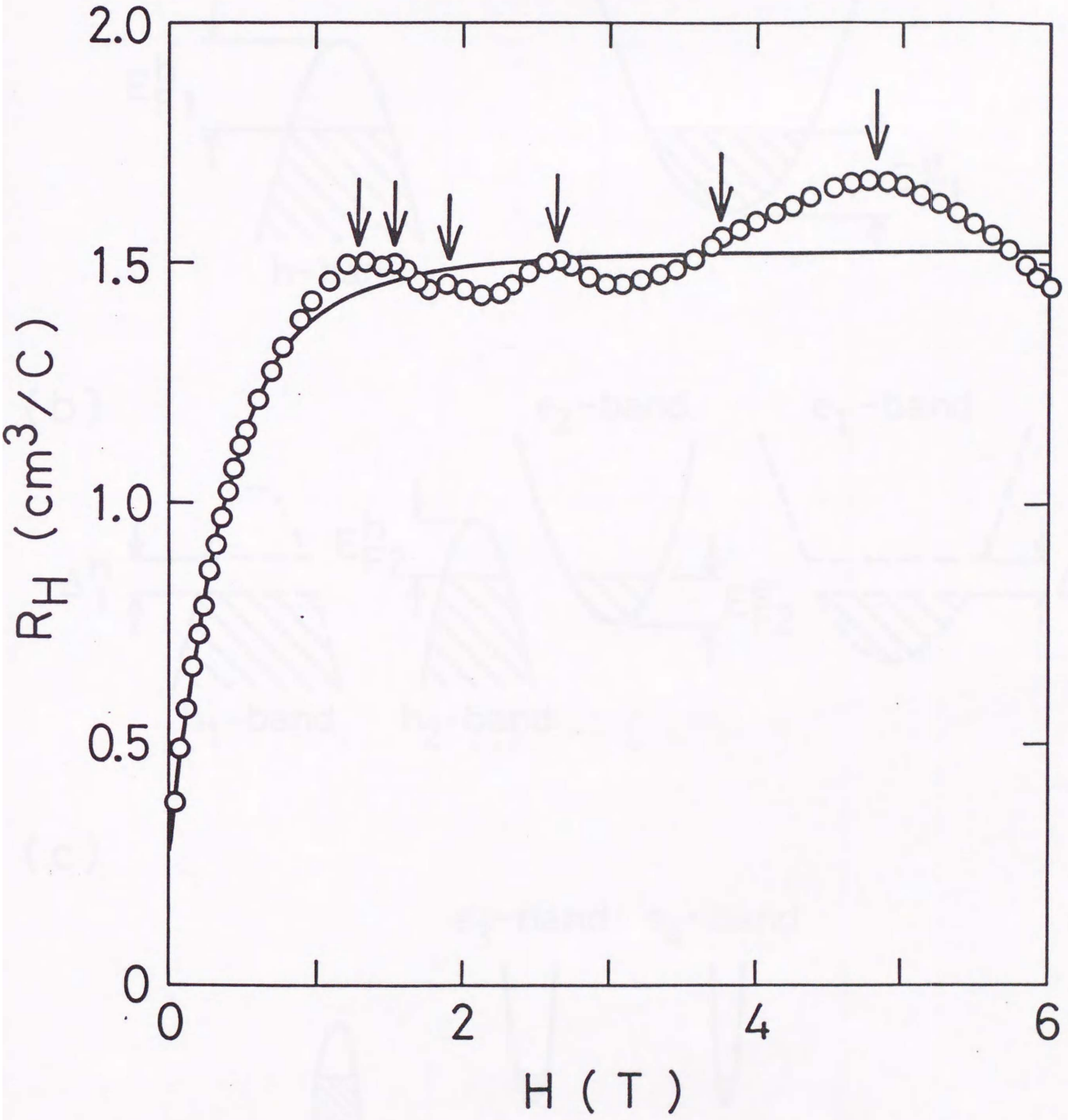

Fig. 15

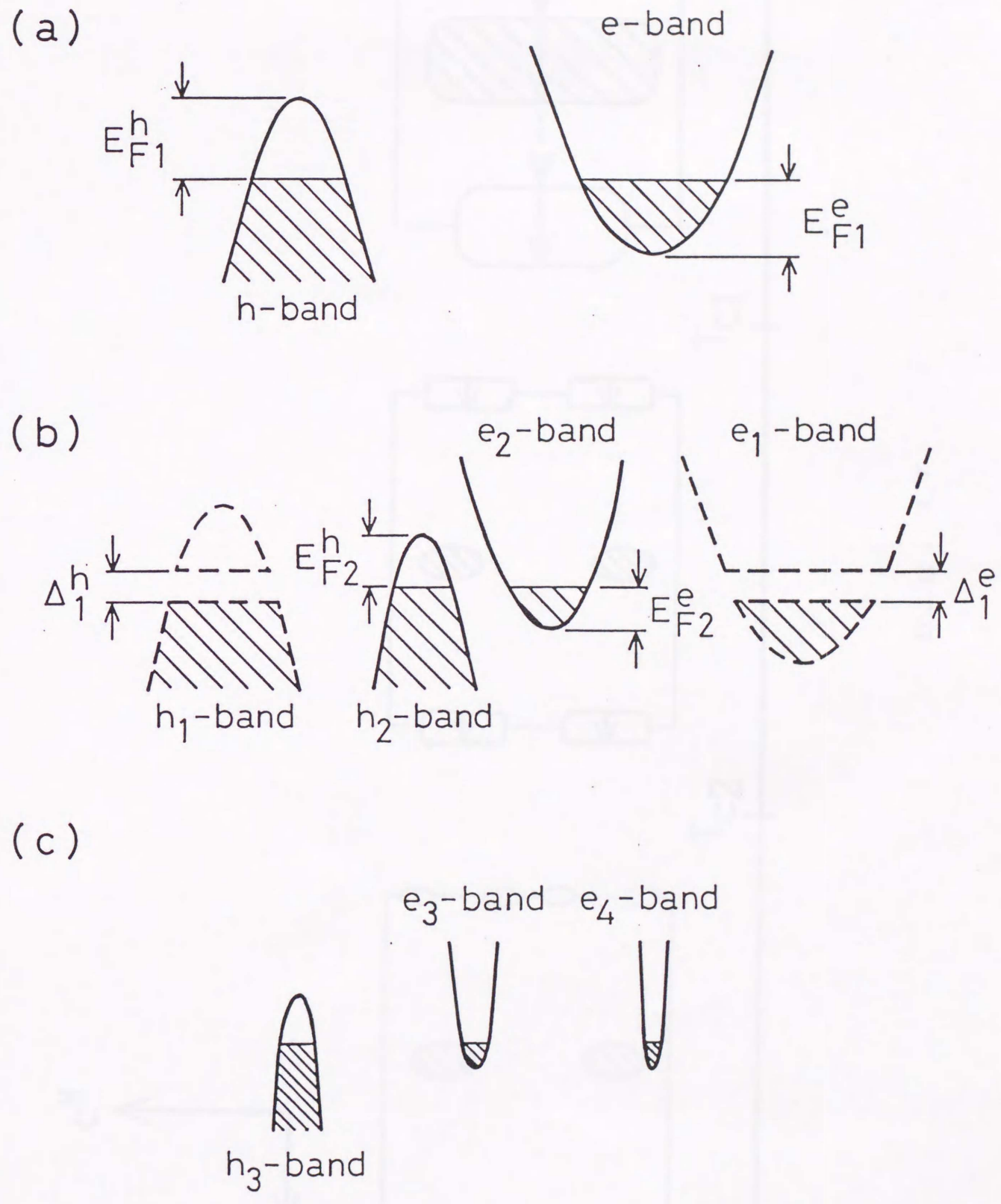
(a)
e-band
E^h_{F1}
E^e_{F1}
h-band
(b)
e_2-band
e_1-band
Δ^h_1
E^h_{F2}
E^e_{F2}
Δ^e_1
h_1-band
h_2-band
(c)
e_3-band
e_4-band
h_3-band

Fig. 16

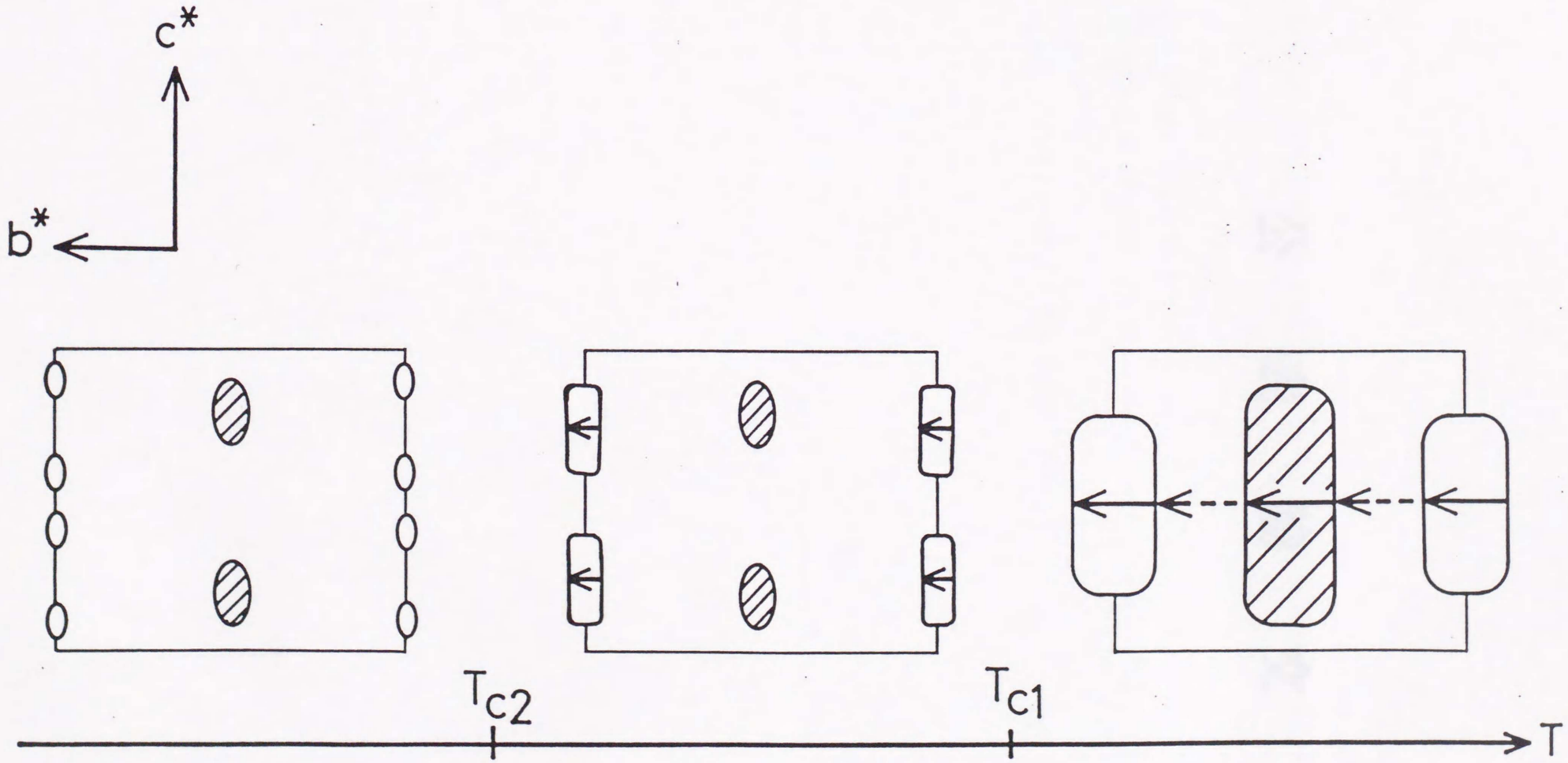

Fig. 17

公　表　論　文

1) M. Inoue, S. Ōhara, S. Horisaka, M. Koyano, and H. Negishi,
Transport Properties of Quasi-Two-Dimentional Mo_4O_{11} Crystals,
phys. stat. sol. (b) 148 (1988) 659.

2) S. Ōhara, M. Koyano, H. Negishi, M. Sasaki, and M. Inoue,
Effect of Pressure on the Charge Density Wave Transitions in η-Mo_4O_{11}
Crystal,
phys. stat. sol. (b) 164 (1991) 243.

参　考　論　文

1) M. Inoue, S. Ōhara, M. Marushita, M. Koyano, H. Negishi, and M. Sasaki, Charge Density Wave Instabilities in Orthorhombic γ-Mo_4O_{11}, Jpn. J. Appl. Phys. 26 (1987) Suppl. 26-3, p. 629.

2) M. Koyano, S. Ōhara, H. Negishi, M. Sasaki, M. Inoue, M. Nomura, and H. Fujiwara, Effect of Pressure on Electrical Resistivity and Crystal Structure of Quasi-Two-Dimentional Mo_4O_{11}, phys. stat. sol. (b) 147 (1988) 559.

3) H. Negishi, S. Ōhara, M. Koyano, M. Inoue, T. Sakakibara, and T. Goto, Anisotropic Spin-Glass and Cluster-Glass of Layered Fe_xTiS_2 Crystals, J. Phys. Soc. Jpn. 57 (1988) 4083.

4) H. Negishi, S. Ōhara, and M. Inoue, Effect of Pressure on Lattice Parameters of Intercalation Compounds M_xTiS_2 (M=Fe and Ni), phys. stat. sol. (b) 151 (1989) 441.

5) M. Koyano, S. Ōhara, S. Horisaka, H. Negishi, M. Inoue, S. Takeyama, and N. Miura, Charge-Density-Wave Related Quantum Transport in Monoclinic η-Mo_4O_{11} Crystal, Solid State Commun. 71 (1989) 317.

6) H. Negishi, K. Sadahiro, S. Ōhara, M. Koyano, M. Sasaki, and M. Inoue, Spin-Glass Behavior in Itinerant Magnetic Material of Fe_xTiS_2, J. Magn. Magn. Mat. 90 & 91 (1990) 345.

7) H. Negishi, S. Ōhara, Y. Takata, T. Yokoyama, M. Taniguchi, and M. Inoue, EXAFS Study of Local Structures in Intercalation Compounds M_xTiS_2 (M=Mn, Fe, Co, Ni), Proc. 6th International Symposium on Intercalation Compounds, May 27-31, 1991, Orleans, France (in press).